J|A|C|S ARTICLES

Published on Web 05/04/2009

Local Membrane Mechanics of Pore-Spanning Bilayers

Ingo Mey,[†] Milena Stephan,[†] Eva K. Schmitt,[‡] Martin Michael Müller,[§] Martine Ben Amar,[§] Claudia Steinem,[‡] and Andreas Janshoff*,[†]

Institute of Physical Chemistry, University of Göttingen, Tammannstrasse 6, 37077 Göttingen, Germany, Institute of Organic and Biomolecular Chemistry, University of Göttingen, Tammannstrasse 2, 37077 Göttingen, Germany, and Laboratoire de Physique Statistique de l'Ecole Normale Supérieure (UMR 8550), associé aux Universités Paris 6 et Paris 7 et au CNRS; 24, rue Lhomond, 75005 Paris, France

Received November 24, 2008; E-mail: ajansho@gwdg.de

Abstract: The mechanical behavior of lipid bilayers spanning the pores of highly ordered porous silicon substrates was scrutinized by local indentation experiments as a function of surface functionalization, lipid composition, solvent content, indentation velocity, and pore radius. Solvent-containing nano black lipid membranes (nano-BLMs) as well as solvent-free pore-spanning bilayers were imaged by fluorescence and atomic force microscopy prior to force curve acquisition, which allows distinguishing between membrane-covered and uncovered pores. Force indentation curves on pore-spanning bilayers attached to functionalized hydrophobic porous silicon substrates reveal a predominately linear response that is mainly attributed to prestress in the membranes. This is in agreement with the observation that indentation leads to membrane lysis well below 5% area dilatation. However, membrane bending and lateral tension dominate over prestress and stretching if solvent-free supported membranes obtained from spreading giant liposomes on hydrophilic porous silicon are indented. An elastic regime diagram is presented that readily allows determining the dominant contribution to the mechanical response upon indentation as a function of load and pore radius.

Introduction

Membrane mechanics plays a pivotal role in many biological processes such as exo- and endocytosis and cell shape/volume regulations. The ability of a lipid bilayer to deform or dilate strongly depends on its chemical composition. To assess quantitative data on the elastic properties of lipid bilayers, mainly nonlocal methods such as micropipet aspiration of giant liposomes have been used.[1,2] However, due to the mosaic nature of biological membranes, it is highly desirable to measure local elastic properties of lipid bilayers on submicrometer length scales. So far, the lack of suitable model systems prevented the use of scanning force techniques to map the elastic properties of membranes in a defined manner. Conventional solid supported lipid bilayers can only be compressed,[3] but bending or stretching requires a second aqueous compartment. With the advent of pore-spanning lipid bilayers, new stable membrane models became available that allow addressing nano- to micrometer sized free-standing membrane patches organized in a well-defined array.[4−9] While classical black lipid membranes (BLMs) lack stability and addressability with local probe microscopy, nano-BLMs − a hybrid between solid supported membranes and BLMs − offer unprecedented mechanical stability over days with mesh sizes between 20 nm and several micrometers in a defined geometric pattern.[10−12] In previous publications, it has been shown that force indentation curves can easily be acquired from the center of the pore. For electrostatically adsorbed *N*,*N*-dioctadecyl-*N*,*N*-dimethylammonium bromide (DODAB) bilayers on mercaptopropionic acid-coated gold-covered porous alumina, we found a rather linear behavior of the force indentation curve, which is dominated by lateral tension,[13] whereas Scheuring and co-workers[14] observed a nonlinear force response attributed to stretching at higher load. Lorenz et al.[15]

[†] Institute of Physical Chemistry, University of Göttingen.
[‡] Institute of Organic and Biomolecular Chemistry, University of Göttingen.
[§] Laboratoire de Physique Statistique de l'Ecole Normale Supérieure (UMR 8550).

(1) Evans, E.; Heinrich, V.; Ludwig, F.; Rawicz, W. *Biophys. J.* **2003**, *85*, 2342–2350.
(2) Rawicz, W.; Olbrich, K. C.; McIntosh, T.; Needham, D.; Evans, E. *Biophys. J.* **2000**, *79*, 328–339.
(3) Künneke, S.; Krüger, D.; Janshoff, A. *Biophys. J.* **2004**, *86*, 1545–1553.
(4) Hennesthal, C.; Drexler, J.; Steinem, C. *ChemPhysChem* **2002**, *3*, 885–889.
(5) Hennesthal, C.; Steinem, C. *J. Am. Chem. Soc.* **2000**, *122*, 8085–8086.
(6) Drexler, J.; Steinem, C. *J. Phys. Chem. B* **2003**, *107*, 11245–11254.
(7) Favero, G.; Capanella, L.; Cavallo, S.; D'Annibale, A.; Perrella, M.; Mattei, E.; Ferri, T. *J. Am. Chem. Soc.* **2005**, *127*, 8103−8111.
(8) Hemmler, R.; Bose, G.; Wagner, R.; Peters, R. *Biophys. J.* **2005**, *88*, 4000–4007.
(9) Han, X. J.; Studer, A.; Sehr, H.; Geissbuhler, I.; Di Berardino, M.; Winkler, F. K.; Tiefenauer, L. X. *Adv. Mater.* **2007**, *19*, 4466–4470.
(10) Römer, W.; Lam, Y. H.; Fischer, D.; Watts, A.; Fischer, W. B.; Göring, P.; Wehrspohn, R. B.; Gösele, U.; Steinem, C. *J. Am. Chem. Soc.* **2004**, *126*, 16267–16274.
(11) Römer, W.; Steinem, C. *Biophys. J.* **2004**, *86*, 955–965.
(12) Schmitt, E. K.; Vrouenraets, M.; Steinem, C. *Biophys. J.* **2006**, *91*, 2163–2171.
(13) Steltenkamp, S.; Müller, M. M.; Deserno, M.; Hennesthal, C.; Steinem, C.; Janshoff, A. *Biophys. J.* **2006**, *91*, 217–226.
(14) Goncalves, R. P.; Agnus, G.; Sens, P.; Houssin, C.; Bartenlian, B.; Scheuring, S. *Nat. Methods* **2006**, *3*, 1007–1012.
(15) Lorenz, B. M.; Mey, I.; Steltenkamp, S.; Fine, T.; Rommel, C.; Müller, M. M.; Maiwald, A.; Wegener, J.; Steinem, C.; Janshoff, A. *Small* **2009**, *5*, 832−838.

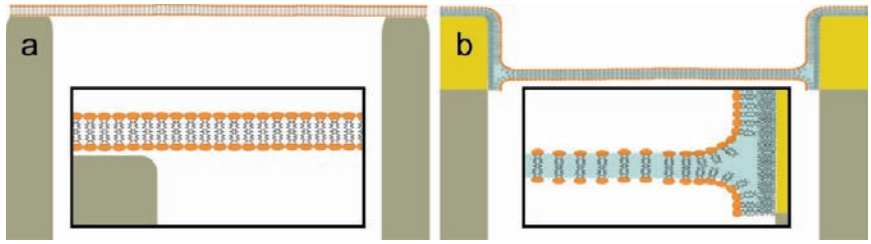

Figure 1. (a) Schematic representation of solvent-free supported bilayers prepared on hydrophilic porous silicon substrates exhibiting negligible prestress. The bilayer on the pore rims can easily slide into the pore upon indentation. The response is bending and tension dominated. (b) Illustration of a hybrid pore-spanning membrane showing substantial prestress. A gold layer of 60 nm (Supporting Information, Figure 1s) on top of the silicon substrate was equipped with a self-assembly layer of octanethiol or CPEO3 prior to membrane deposition either via painting of lipids or spreading of giant liposomes.

also found a nonlinear indentation response of native cell membranes predominately due to bending and lateral tension.

The question arises how the lipid composition and surface functionalization as well as pore radius, tip size, and solvent content determine the mechanical response of pore-spanning bilayers, and how the system can be tuned to measure and extract intrinsic elastic properties of biomembranes. To address these questions, we performed indentation experiments on pore-spanning lipid bilayers with an atomic force microscope (AFM)-tip and varied the pore radius of the underlying substrate, the surface functionalization, solvent content, lipid composition, and loading rate. We present a theoretical model to answer the question whether bending, prestress, or stretching dominates the membranes' mechanical response. We found that prestress is the decisive parameter, which governs the mechanics of pore-spanning membranes that are attached to a hydrophobically functionalized porous substrate, while bending *and* lateral tension dominate the mechanical response of solvent-free supported pore-spanning bilayers on porous Si/SiO_2. From our analysis, we infer a recipe that allows to enhance the mechanical stability of pore-spanning bilayers by using different self-assembly strategies.

Materials and Methods

Preparation of Substrates. Porous silicon substrates from fluXXion B.V. (Eindhoven, NL) with pore radii of 225, 400, and 600 nm were used if not indicated otherwise. Prior to use, the substrates were cleaned in an argon plasma for 30 s (Plasma Cleaner, Harrick Plasma, Ithaca, NY). Then, 3 nm of chromium and 60 nm of gold were evaporated at a rate of 0.1 nm/s onto the substrates. Prior to monolayer formation, the substrates were again cleaned in an argon plasma for 30 s and incubated in a 2 mM ethanolic octanethiol solution or a 0.2 mM *n*-propanolic cholesterylpolyethylenoxy thiol solution overnight at room temperature. After rinsing with ethanol and buffer, the substrates were subjected to the nano-BLM formation procedure. For preparation of supported solvent-free pore-spanning lipid bilayers obtained from spreading of giant unilamellar vesicles (GUVs), custom-made porous substrates from NFT GmbH (Munich, Germany) with a smaller porosity were used to facilitate vesicle spreading.

Preparation of Nano Black Lipid Membranes (nano-BLMs). First, lipid solutions in organic solvents were prepared with the following concentrations: 4 mg/mL 1,2-diphytanoyl-*sn*-glycero-3-phosphocholine (DPhPC) in *n-decane*; 0.1 mg/mL 1,2-dipalmitoyl-*sn*-glycero-3-phosphocholine (DPPC, Avanti Polar Lipids, Alabastar, AL) with or without cholesterol (Sigma-Aldrich, Taufkirchen, Germany) in *octane/dodecane* (3:2). To visualize nano-BLMs with an upright fluorescence microscope, the solutions were doped with either 0.1 mol % of 2-(4,4-difluoro-5-methyl-4-bora-3a,4a-diaza-*s*-indacene-3-dodecanoyl)hexadecanoyl-*sn*-glycero-3-phosphocholine (BODIPY-PC, Invitrogen, Karlsruhe, Germany) or 0.1 mol % sulforhodamine-1,2-dihexanoyl-*sn*-glycero-3-phosphoethanolamine (TexasRed-DHPE, Sigma-Aldrich, Taufkirchen, Germany).

Prior to nano-BLM formation, the functionalized porous substrates were rinsed first with pure ethanol and then with a 1:1 mixture of ethanol/water (Gradient A10, Sartorius AG, Göttingen, Germany) to prevent the entrapment of air bubbles in the pores. After 10 min, the ethanol/water mixture was exchanged with a 0.1 M NaCl solution. With a paint brush, a small amount of lipid dissolved in organic solvent was deposited on the substrate, and lipid bilayers were formed as a result of the thinning process. Experiments were started 60 min after the lipid−solvent droplet has been applied to the functionalized porous substrate to allow the thinning process to take place and to minimize residual solvent in the membrane. We refer to these pore-spanning membranes attached to a hydrophobic self-assembled monolayer on a porous substrate as *hybrid (solvent-containing) pore-spanning membranes* (Figure 1b).

Preparation of Solvent-Free Pore-Spanning Bilayers. GUVs, prepared by electroformation, were spread on functionalized porous substrates to form solvent-free pore-spanning bilayers. One hundred microliters of a 10 mg/mL DPhPC or DPPC solution, doped with 1 mol % of TexasRed-DHPE or BODIPY-PC, dissolved in chloroform were uniformly deposited on two indium tin oxide (ITO)-coated glass slides (Praezisions Glas & Optik GmbH, Iserlohn, Germany) using a syringe. Under vacuum, the solvent was evaporated above the main-phase transition temperature of the lipids overnight to produce solvent-free lipid films. With a copper tape the ITO-slides were contacted with a waveform generator (Wavetek, model 23), and a compartment around the lipid films was formed with a sealing agent (Hematokrit sealing filler schuett24, Göttingen, Germany). The compartment was filled with 1 mL of ultrapure water. At a temperature above the main-phase transition temperature of the lipid, an ac current at a frequency of 10 Hz and a peak-to-peak amplitude of 5 V was applied, which resulted in the formation of GUVs.[16] After 90 min, a sufficient number of GUVs was formed, and the GUV suspension was stored at 4 °C prior to use. GUVs were stable up to 7 days when stored at 4 °C.

The functionalized porous substrates were rinsed with pure ethanol and a 1:1 mixture of ethanol/water. The ethanol/water mixture was then exchanged with a 0.1 M NaCl solution. Five hundred microliters of the GUV suspension was deposited on the substrate and the temperature was increased above the phase transition of the lipid vesicles to induce spreading. We refer to pore-spanning membranes attached to a hydrophobic self-assembled monolayer on a porous substrate as *hybrid (solvent-free) pore-spanning membranes* (Figure 1b).

Besides GUVs spread on functionalized porous silicon substrates, they were also spread directly on hydrophilic porous silicon oxide surfaces. Prior to GUV spreading, the substrates were hydrophilized by incubating first in a 1% aqueous HF solution followed by incubation in a solution containing $NH_3/H_2O_2/H_2O$ (1:1:5). A fresh layer of silicon dioxide is formed with a thickness of a few nanometers. Substrates were rinsed with a 1:1 mixture of ethanol/water. After 10 min, the mixture was exchanged with a solution of

(16) Bagatolli, L. A.; Parasassi, T.; Gratton, E. *Chem. Phys. Lipids* **2000**, *105*, 135–147.

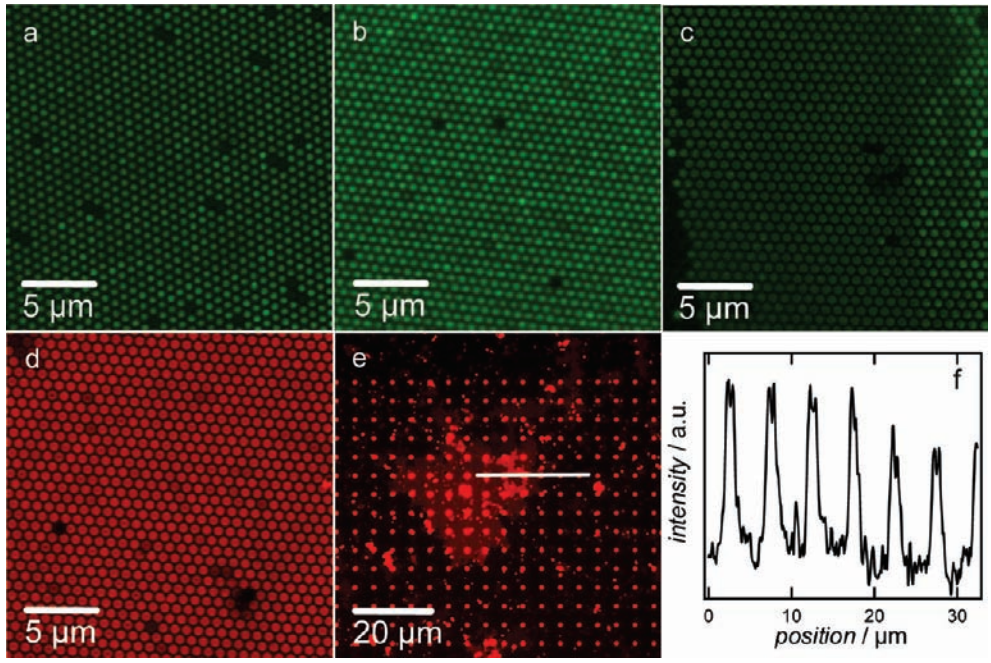

Figure 2. Fluorescence images of different pore-suspending membranes. (a) nano-BLMs composed of DPhPC/BodiPyPC (99:1) on an octanethiol (OT)-monolayer (pore radius: 400 nm); (b) nano-BLMs composed of DPhPC/BodiPyPC (99:1) on a CPEO3-monolayer (pore radius: 400 nm); (c) nano-BLMs composed of DPhPC/BodiPyPC (99:1) on OT (pore radius: 600 nm); (d) nano-BLMs composed of DPPC/TexasRed-DHPE (99:1) on an OT-monolayer at room temperature (pore radius: 600 nm); (e) solvent-free supported DPhPC/TexasRed-DHPE (99:1) bilayer on porous silicon with pore radii of 250 nm. Without the gold layer, the pores exhibit photoluminescence, which is enhanced if pore-spanning bilayers are present. The line scan in (f) shows the increase in fluorescence intensity on the membrane-covered pores.

0.2 M NaCl, 2 mM $CaCl_2$. One milliliter of the DPhPC GUV suspension was mixed with 1 mL of 0.2 M NaCl, 2 mM $CaCl_2$ solution and deposited on the substrate. Spreading of vesicles on the surface leads to *solvent-free supported bilayers* within 2 h. The membranes consist of two identical leaflets as schematically illustrated in Figure 1a.

Fluorescence Microscopy. An upright optical microscope (Olympus BX-51, Olympus Germany GmbH, Hamburg, Germany) equipped with filter sets for BODIPY and TexasRed fluorescence (U-MNB2 and UMNG2, Olympus Germany GmbH, Hamburg, Germany) and water immersion objectives with 40× (Olympus, LUMPlanFl 40XW, N.A. = 0.8), and 100 × (Olympus, LUMPlanFl 100W, N.A. = 1.00) magnification were used for fluorescence inspection of the pore-spanning membranes. By using the microscopic grid displayed by the porous substrates, we were able to determine the exact coordinates of the observed position.[15] These coordinates were used for a correlation with atomic force microscopy images.

Atomic Force Microscopy (AFM). Experiments were performed on a MFP-3D (Asylum Research, Santa Barbara, CA) AFM equipped with a top view optic, using silicon nitride tips MSCT-AU, DNP-S both purchased from Veeco Instruments (Mannheim, Germany), and Biolever™ obtained from Olympus with nominal spring constants of 0.01, 0.06, and 0.006 N/m with nominal tip radii of 10 and 30 nm (Biolever). The grid structure of the porous substrates was observable with the top view optic and an area, which was identified by fluorescence microscopy, was chosen for AFM experiments. Exact spring constants of the cantilevers were determined by the thermal noise method.[17]

Results and Discussion

Visualization of Pore-Spanning Bilayers. Three different preparation techniques of pore-spanning bilayers were employed and compared. First, phospholipids dissolved in organic solvent were spread on hydrophobic self-assembly layers chemisorbed on gold-covered porous silicon substrates resulting in so-called nano-BLMs.[12,18] The highly ordered silicon substrates exhibit pore radii ranging from 225−600 nm and display a hydrophobic monolayer composed of either octanethiol (OT) or cholesterylpolyethylenoxy thiol (CPEO3). Second, solvent-free pore-spanning membranes were obtained from spreading of GUVs on a hydrophobic monolayer composed of OT or CPEO3. Both preparation procedures have in common that the first membrane leaflet on the solid support is provided by the self-assembly layer and are thus summarized as *hybrid pore-spanning membranes*. The third method uses hydrophilic nonfunctionalized porous silicon chips, on which giant liposomes were directly spread to form planar pore-spanning bilayers, which we refer to as *solvent-free supported bilayers* (Figure 1).

Successful formation of pore-spanning bilayers was verified by fluorescence (Figure 2) and AFM imaging (Figure 3). Figure 2 shows fluorescence images of nano-BLMs composed of DPhPC (Figure 2a-c) and DPPC (Figure 2d) at room temperature, respectively. The majority of pores are covered by a membrane showing a bright fluorescence. The few dark spots in the array are noncovered pores. Notably, BODIPY-PC and TexasRed-DHPE fluorescence is quenched on the gold-covered rims,[18] which allows the assignment of each individual pore. Prior to each AFM experiment, fluorescence images were taken to confirm bilayer formation on the pores. Figure 2e shows a fluorescence image of giant liposomes spread on the hydrophilic porous silicon substrate. The pores themselves are photoluminescent, and the additional fluorescence indicates successful formation of pore-spanning bilayers as illustrated by the line

(17) Butt, H. J.; Jaschke, M. *Nanotechnology* **1995**, *6*, 1–7.

(18) Weiskopf, D.; Schmitt, E. K.; Klühr, M. H.; Dertinger, S. K.; Steinem, C. *Langmuir* **2007**, *23*, 9134–9139.

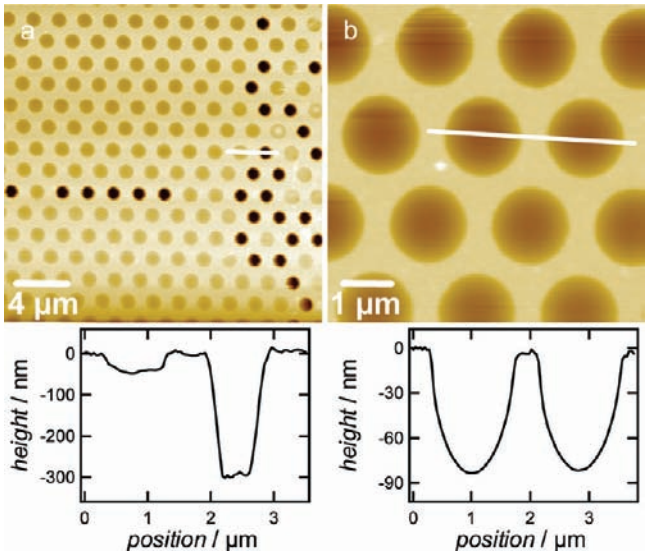

Figure 3. AFM (contact mode) images of different pore-suspending membranes. (a) Nano-BLMs composed of DPhPC on OT (pore radius: 400 nm). The load force was 100 pN. Some pores (black holes) are not covered with a membrane (b) Nano-BLMs composed of DPhPC on OT (pore radius: 600 nm). The load force was 300 pN. All pores are covered with membranes in this image.

scan in Figure 2f. AFM images confirm that, indeed, single bilayers were spread on the substrate (Supporting Information).

By means of AFM, the topography of the functionalized surface was monitored, and a first judgment, whether the membranes withstand contact with the AFM-tip, could be made. Topographic images obtained in contact mode with a load force of 300 pN unambiguously reveal pore-spanning DPhPC bilayers (Figure 3a). Membrane-covered and uncovered pores can be readily distinguished. The height profile taken from the white solid line in Figure 3a demonstrates that a membrane suspending a single pore is indented only up to 70 nm, while the cantilever tip reaches a depth of nearly 300 nm in an uncovered pore with a pore radius of 225 nm. In general, pore size and tip geometry govern the maximal indentation depth upon imaging. A pore radius of 225 nm allows a maximal indentation of 400 nm, while a pore radius of 400 nm exhibits indentations depths up to 550 nm. Finally, a pore radius of 600 nm shows an indentation depth of 650 nm. The tip size (radius of apex) was 15−25 nm for all experiments as determined by scanning electron microscopy.

Scanning across the membrane-covered pores is invasive as illustrated in panels a/b in Figure 4, which display two consecutive contact mode AFM images obtained at a load force of 300 pN. A few membranes rupture during the imaging process (Figure 4a). Remarkably, they rupture most likely when the AFM tip reaches the center of the pore. The subsequent AFM image of the same area (Figure 4b) displays the corresponding pattern of noncovered pores consistent with the membrane rupturing that occurred during the first scan. In order to rule out that AFM imaging does not visualize all pore-spanning bilayers, we generated overlay images of fluorescence and topography images (Figure 4c). The pattern of uncovered (nonfluorescent) and membrane-covered (fluorescent) pores is identical and hence confirms that AFM imaging faithfully reproduces the existence of pore-spanning bilayers as well as uncovered pores. The line profiles (Figure 4d) demonstrate the small indentation of the tip into the pore of about 70 nm if a membrane covers the pore (black line), simultaneously reproduced by the increased fluorescence intensity (green line).

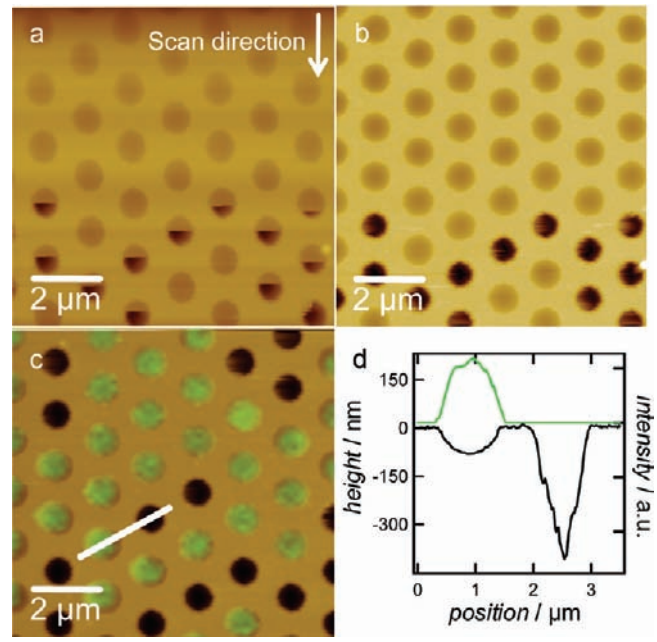

Figure 4. AFM images and fluorescence/AFM correlation of painted DPhPC nano-BLMs on pores with radii of 400 nm. (a) Topographic AFM image (contact mode) obtained at a loading force of 300 pN showing rupture events during the first AFM scan. (b) Second scan also at a loading force of 300 pN displaying the pattern of open pores occurred after the first scan. (c) Overlay of fluorescence (green) and AFM topography (brown) images of DPhPC/BodipyPC (99:1)/OT nano-BLMs on a porous silicon substrate with a pore radius of 400 nm. (d) Height and fluorescence profiles (along white line in (c)) of a membrane-covered and uncovered pore.

Force Indentation Measurements. Force indentation experiments with a force resolution of <10 pN were repeatedly carried out in the center of the membrane-covered pores to measure the elastic response of the membranes. In all cases, the response of the membrane was fully elastic; trace and retrace curves did not show a hysteresis indicative of energy dissipation. We also varied the loading rate between 1−1000 nN/s (Supporting Information) while indenting the same nano-BLM repeatedly. Within this loading rate range, the slopes of the force indentation curves are indistinguishable up to the point of rupture. No dependency of the loading rate on the mechanical response is found supporting the fully elastic behavior of the membranes.

Typical force indentation curves obtained from membranes with various lipid compositions and solvent content, immobilized on differently functionalized surfaces with different pore diameters are compiled in Figure 5. Force distance curves acquired on the pore rim (red curve) as well as force indentation curves obtained from the center of the pore (black curve) are displayed. Since cantilever bending might produce a number of artifacts when the tip touches the pore wall at its side and not with the apex, it is mandatory to extract the inverted optical lever sensitivity (INVOLS) and a reference for the point of contact from the force distance curves obtained from the pore rim. The point of contact between membrane and cantilever tip is 70 nm below the pore rim (zero point) as already suggested by the topographical AFM images shown in Figure 3. As a 60 nm thick gold layer was evaporated onto the porous substrate, we envision a situation as schematically illustrated in Figure 1b. This finding is corroborated by a recent study of Böcker et al.[19] using noninvasive scanning ion conductance microscopy.

The response of the nano-BLMs as well as the solvent-free hybrid pore-spanning bilayers to the indentation is predominately

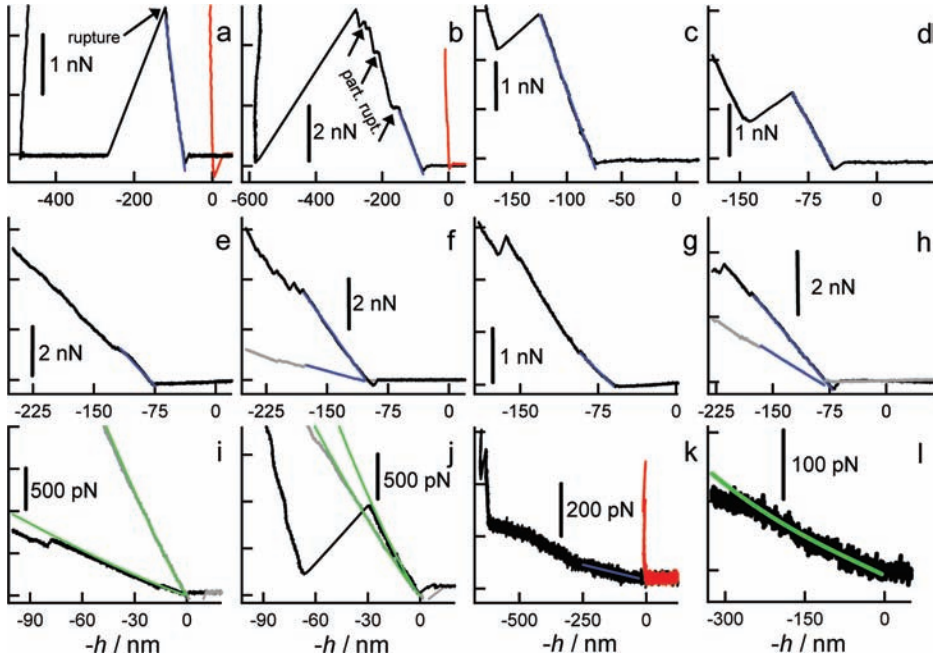

Figure 5. Representative collection of force indentation curves obtained from various hybrid pore-spanning membranes and solvent-free supported DPhPC bilayers. Surface functionalization, pore radius, and solvent content of the membranes were varied. The following legend indicates phospholipid/surface functionalization/pore radius/preparation method (bilayers from lipid-solvent painting or GUV spreading (GUV)) and the corresponding apparent spring constant k_{app} (blue line). (a) DPhPC/OT/400/*n*-decane, $k_{app} = 40$ mN/m; the arrow indicates the rupture point of the membrane. (b) DPhPC/OT/600/*n*-decane, $k_{app} = 28$ mN/m; the arrows indicate partial rupture events. (c) DPhPC/OT/225/*n*-decane, $k_{app} = 52$ mN/m. (d) DPhPC/CPEO3/400/*n*-decane, $k_{app} = 30$ mN/m. (e) DPhPC/OT/600/GUV, $k_{app} = 34$ mN/m. (f) DPPC/OT/600/octane/dodecane (gray line: $T = 50$ °C, $k_{app} = 8$ mN/m, black line: $T = 21$ °C, $k_{app} = 44$ mN/m). (g) DPPC/OT/600/GUV at 50 °C, $k_{app} = 20$ mN/m. (h) DPPC/Chol(75:25)/OT/600/octane/dodecane (gray line: $T = 50$ °C, $k_{app} = 14$ mN/m, black line: $T = 20$ °C, $k_{app} = 27$ mN/m). (i) black line: DPPC/OT/600/octane/dodecane at 50 °C, gray line: DPPC/OT/600/octane/dodecane, the green curve represents calculated force indentation curves using eq 6 with the following parameters: $R_{pore} = 600$ nm, $R_{tip} = 15$ nm, black: $\sigma = 8$ mN/m, gray: $\sigma = 30$ mN/m. (j) gray line: DPhPC/OT/600/*n*-decane, black line: DPhPC/OT/225/*n*-decane, green line: fit according to eq 6 with the following parameters for the gray curve: $R_{pore} = 600$ nm, $R_{tip} = 15$ nm, $\sigma = 17$ mN/m, and for the black curve: $R_{pore} = 225$ nm, $R_{tip} = 15$ nm, $\sigma = 19$ mN/m. (k/l) Solvent-free supported membranes (DPhPC) on silicon substrates with a pore radius of 250 nm, $k_{app} = 230$ μN/m (blue line in (k)). Force indentation curve taken on the rim is shown in red. (l) Green curve: calculated force distance curve using eq 5 with the following parameters: $R_{pore} = 250$ nm, $R_{tip} = 15$ nm, $\sigma = 100$ μN/m, $\kappa = 1.17 \times 10^{-19}$ J.[30]

Table 1. Apparent Spring Constants k_{app} and Corresponding σ of Various Pore-Spanning Bilayers[a]

lipid	R_{pore} / nm	surface	k_{app} / mN m^{-1}	σ/mN m^{-1}
DPhPC	225	OT	48 ± 15	22 ± 6
DPhPC	400	OT	36 ± 8	21 ± 4
DPhPC	400	CPEO3	26 ± 5	15 ± 3
DPhPC	600	OT	25 ± 6	18 ± 3
DPPC	600	OT	40 ± 4	31 ± 3
DPPC/Chol	600	OT	31 ± 4	23 ± 3
DPPC[b]	600	OT	9 ± 2	7 ± 1
DPPC/Chol[b]	600	OT	14 ± 3	11 ± 3
DPPC[b,c]	600	OT	21 ± 3	16 ± 2
DPhPC[c]	600	OT	34 ± 5	26 ± 4
DPhPC[d]	250	SiO_2	0.21 ± 0.05	0.15 ± 0.05

[a] The tension σ is interpreted as prestress or apparent lateral tension originating from differences in the chemical potential of the lipid reservoir and the indented free-standing bilayer. [b] At 50 °C. [c] Spreading of GUVs on chemisorbed thiols on gold-covered porous substrates. [d] Spreading of GUVs on clean porous silicon dioxide samples.

linear. This allows us to define and extract an apparent spring constant[13] $k_{app} = -(dF/dh)_{\rho=0}$ for each membrane (Table 1).

Rupture events are frequently visible at penetration depths of 20−150 nm identified as a sudden drop of the restoring force to zero (see Figure 7). Infinite repulsion is observed when hitting the pore walls at maximal indentation depth limited by pore and tip geometry. Several instabilities are visible upon indentation, which we attribute to incomplete rupture events (see Figure 5b). It is conceivable that not all rupture events inevitably lead to disintegration of the whole membrane as schematically illustrated in Figure 6c. Frequently, force indentation curves on pore-spanning membranes display several breakthrough events after a few up to several tens of nanometers of indentation into the pore (Figure 5). There are various scenarios that can be envisioned how the membrane ruptures (Figure 6). The tip applies a force on a local scale, which results in the formation of a pore in the contact regime between lipid bilayer and tip (Figure 6c). When the hole in the membrane reaches a certain critical radius, membrane rupture occurs and the pore-spanning lipid bilayer gets locally destroyed (Figure 6d). However, it is also conceivable that membrane rupturing occurs away from the contact region between tip and membrane as a consequence of the stochastic nature of membrane rupture (Figure 6e). If the membranes are completely disrupted by the AFM tip, the cantilever immediately relaxes and the force response resembles that of a tip approaching an uncovered pore, i.e. the tip hits the pore walls several hundred nanometers below the surface. This is frequently found as depicted in Figure 5a. However, rupture events also occur without destruction of the membrane. This finding might be explained by a partial breakthrough as shown in Figure 6c. It is also possible that a small hole forms due to penetration of an imperfect tip, leading to only short relaxation of the cantilever (Figure 6f).

The absolute area increase or dilatation of the membranes at the point of rupture is calculated by assuming that the indented

(19) Böcker, M.; Muschter, S.; Schmitt, E. K.; Steinem, C.; Schäffer, T. E. *Langmuir* **2009**, *25*, 3022–3028.

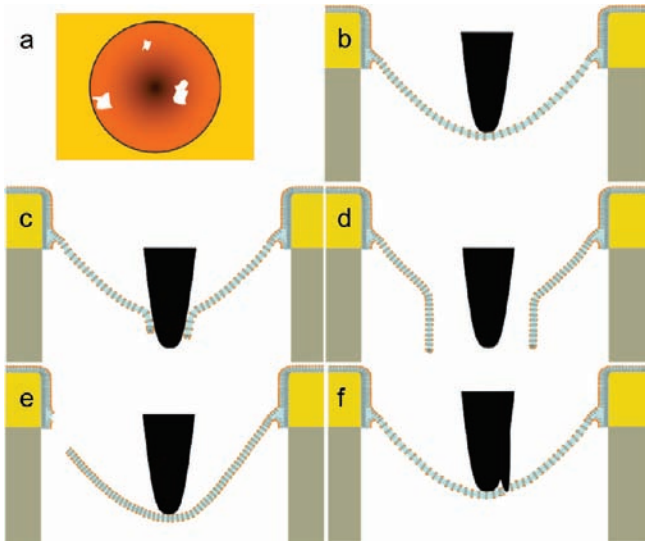

Figure 6. Illustration of conceivable pathways of membrane rupture upon indentation. (a) Top view of a pore-spanning bilayer with local membrane rupture. (b) Lateral view of the indentation of a prestressed hybrid pore-spanning membrane on a gold-covered substrate. Due to the gold film on top of the silicon substrate, the membrane is formed below the pore rim. (c) A hole forms in the center, and the tip slides through this defect. The attached membrane stays intact and relaxes slightly. (d/e) Possible stochastic rupture events. (f) Inhomogeneities of the tip morphology (here double tip) may enforce a partial breakthrough of the tip.

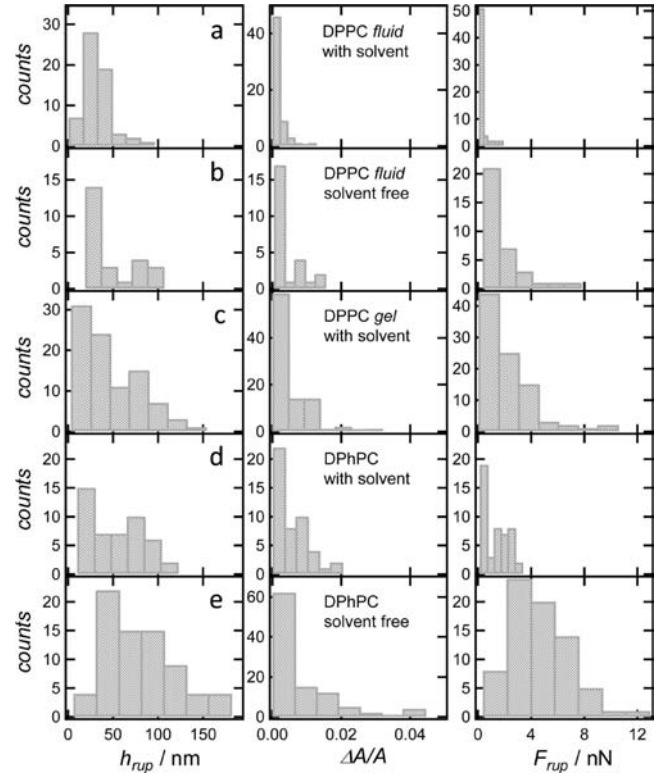

Figure 7. Histograms of the maximal indentation depths in the center of the pore up to rupture h_{rup}, the relative area dilatation $\Delta A/A$ of the bilayer, and its rupture forces F_{rup} (first breakthrough/rupture event) as a function of the pore-spanning bilayer preparation. The following legend indicates phospholipid/surface functionalization/pore radius/preparation method (bilayers from lipid/solvent painting (octane/dodecane) or GUV spreading (GUV)) (a) DPPC/OT/600/octane/dodecane at $T = 50$ °C, (b) DPPC/OT/600/GUV at $T = 50$ °C, (c) DPPC/OT/600/octane/dodecane at $T = 21$ °C, (d) DPhPC/OT/600/*n*-decane, (e) DPhPC/OT/600/GUV.

membranes adopt the geometry of a simple cone, which is a valid approximation for small R_{tip}/R_{pore} ratios. We found that breakthrough events occur mainly if the bilayer is stretched by 0−2% (Figure 7). Area dilatation of more than 5% was generally not found. Since in a very large number of experiments first rupture events occur at very low area dilatation (approximately 1% and lower), it is likely that a lateral tension is homogenously acting on the membrane causing a prestrain of the free-standing lipid bilayer. This issue is discussed in detail in the next section.

Origin of the Elastic Response: Theoretical Considerations. In principle, the elastic response of the system comprises three major contributions: bending, stretching, and lateral tension (e.g., prestress). Assuming a point load force as it is justified for the rather large pore sizes and small tip radii used in this study, a membrane response based on pure bending produces very small restoring forces following thin plate theory. Solving $F = -\partial H/\partial h$ for the small gradient approximation of the bending energy $H = \pi \int_0^{R_{pore}} d\rho\ \rho[\kappa(\Delta h)^2]$ we obtain the following linear relationship for a point load force (eq 1):[20]

$$F(h) = \frac{4\pi E t^3}{3(1-\nu^2)R_{pore}^2} h = \frac{4\pi}{3}\frac{48\kappa}{R_{pore}^2} h \qquad (1)$$

E denotes the elastic modulus (Young's modulus), ν the Poisson ratio, R_{pore} the pore radius, h the indentation depth, and t the thickness of the bilayer. Assuming reasonable values for E such as 28 MPa, $\nu = 0.33$, and a thickness of $t = 5.5$ nm, which corresponds to a bending modulus of $\kappa = 1.1 \times 10^{-19}$ J for the membrane, we obtain an apparent spring constant of the bilayer in the range of 4×10^{-5} N/m. Table 1 compiles the measured apparent spring constants for the various membrane preparations. Except for solvent-free supported bilayers attached to nonfunctionalized porous silicon substrates, all k_{app} values exceed 10^{-3} N/m by far. It can thus safely be assumed that bending is only a very minor contribution to the indentation response of hybrid pore-spanning membranes. Only in case of solvent-free supported bilayers is k_{app} considerably smaller, so that the elastic response is governed by bending *and* lateral tension. Moreover, these solvent-free supported bilayers show no rupture events ruling out stretching as the major source of restoring force.

Stretching is a major contribution to the elastic response at larger indentation forces. Generally, this regime is described by the so-called membrane theory. The membrane regime is characterized by displacements proportional to the cube root of the applied load. It is well-known that the area dilatation $\Delta A/A$ of membranes in two dimensions follows a simple 2-D Hookean law $\sigma = K_a(\Delta A)/(A)$, with tension σ and the area compressibility K_a ($K_a \approx tE$).[21,22] From $H = \int \sigma\, dA$ we obtain the following cubic dependence on the penetration depth for the force indentation curve (eq 2):[14,20]

$$F(h) = g(\nu) R_{pore} E t \left(\frac{h}{R_{pore}}\right)^3 \qquad (2)$$

where $g(\nu) = \pi/3$ for $\nu = 0.33$. Since most experimental force indentation curves show a predominately linear dependence on the indentation depth (see Figure 5), this contribution alone does not explain our findings. Notably, membrane rupture generally

(20) Komaragiri, U.; Begley, M. R. *J. Appl. Mechanics-Trans. ASME* **2005**, *72*, 203–212.
(21) Evans, E.; Rawicz, W. *Phys. Rev. Lett.* **1990**, *64*, 2094–2097.
(22) Needham, D.; Hochmuth, R. M. *Biophys. J.* **1989**, *55*, 1001–1009.

occurs if area dilatation exceeds 3−5%.[23,24] Since frequently observed rupture events are caused most likely by area dilatation, lateral stretching occurs eventually at larger deformations.

A possible scenario, which explains all observations, needs to include a third contribution, namely prestress, to the elastic response of the membrane. In the case of hybrid pore-spanning membranes, the hydrophobic monolayer causes a situation, in which the membrane is strained due to stress originating from the hydrophobic effect. The reduction in free energy on the hydrophobic self-assembly layer creates a homogeneous and constant prestress (σ). Solving the corresponding Euler−Lagrange equation $\sigma\Delta h = F/\pi R_{\text{pore}}^2$ leads to a linear relationship between force and indentation depth assuming a homogeneous pressure on the membrane (eq 3):[25]

$$F = 4\pi\sigma h \tag{3}$$

Interestingly, eq 3 does not depend on the pore radius, and k_{app} would directly reflect the prestress in the membrane. As a working hypothesis, we assume that force indentation curves of hybrid pore-spanning membranes are a linear combination of stretching and repulsion due to prestress. What are the consequences if prestress governs the mechanical response? If prestress is responsible for the observed linear relationship between force and penetration depth, the maximal area dilatation should be well below 3−5%, and the impact of pore radii should be small. Another question might be how the finite tip size changes the scaling laws.

To answer those questions, we scrutinized the rupture behavior of pore-spanning bilayers. Figure 7 shows a collection of histograms displaying the distributions of the indentation depth, at which the first rupture event was observed (h_{rup}), of the area dilatation until the first rupture event ($\Delta A/A$), and of the rupture force (F_{rup}). The area is calculated from a conical shape function.

$$A = \pi R_{\text{pore}}\sqrt{R_{\text{pore}}^2 + h^2} - \pi R_{\text{pore}}^2$$

Importantly, we found not a single rupture event that exceeds an area dilatation of 4% in accordance with the maximal possible area dilatation of around 5%. Most events were observed below an area dilatation of 1% supporting our assumption that the membrane is in a prestressed state.

So far, we only considered point load forces and homogeneous pressure loads to illustrate our argument that hybrid pore-spanning membranes withstand external force due to their prestressed state. The finite size of the tip has entirely been ignored. The small gradient approximation provides the following Hamiltonian (eq 4):

$$H_{\text{lin}} = \pi \int_0^{R_{\text{pore}}} \mathrm{d}\rho\, \rho[\kappa(\Delta h)^2 + \sigma(\nabla h)^2] \tag{4}$$

with the corresponding Euler−Lagrange equation:

$$\Delta\left(\Delta - \frac{\sigma}{\kappa}\right)h = 0$$

Following the arguments outlined in Steltenkamp et al.[13] and Norouzi et al.[27] we obtain eq 5:

$$F = -\mathbf{e}_{\text{h}} \cdot \oint_\gamma \mathrm{d}s(l_a \mathbf{f}^a) = 2\pi R_{\text{pore}} \times \kappa \left.\frac{\partial K}{\partial \rho}\right|_{\rho = R_{\text{pore}}}, \; a \in \{1, 2\} \tag{5}$$

Here, $\mathbf{f}^a$ is the surface stress tensor, l_a the outward pointing unit normal of the line element ds of γ, and $\mathbf{e}_{\text{h}}$ is the unit vector normal to the substrate. The integral runs along the rim of the pore, where $\rho = R_{\text{pore}}$. Using the shape function to calculate the derivative of the curvature K at the rim yields the force acting normal on the membrane. σ can be interpreted as either the apparent lateral tension arising due to a difference in the chemical potential between the lipid reservoir and the indented bilayer or the prestress of the bilayer.

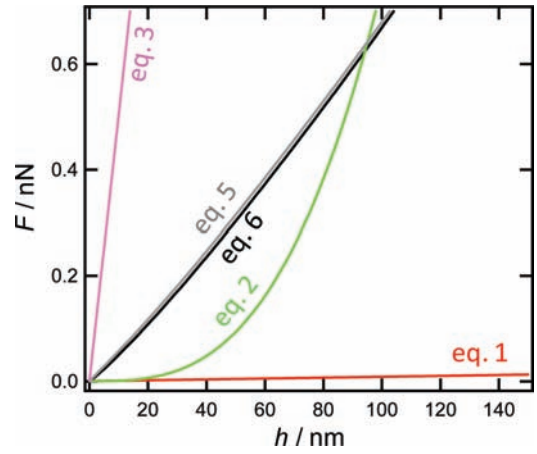

Figure 8. Calculations of different possible elastic responses upon membrane indentation according to eqs 1–3 and 5–6. The following parameters were used: $R_{\text{pore}} = 600$ nm, $R_{\text{tip}} = 20$ nm, $t = 5$ nm, $\sigma = 4$ mN/m, $\kappa = 1.5 \times 10^{-19}$ J, $\nu = 0.33$.

Neglecting bending of the membrane as argued above leads to an analytical expression as pointed out by Bhatia and Nachbar[26] as well as Deserno and co-workers[27] (eq 6):

$$h = \frac{F}{4\pi\sigma}\left[1 - \ln\left(\frac{FR_{\text{tip}}}{2\pi\sigma R_{\text{pore}}^2}\right)\right] \tag{6}$$

Begley et al.[28] provide a force indentation relationship for a spherical indenter using membrane theory assuming zero prestretch and obtain eq 7:

$$F = \frac{9\pi E t}{16 R_{\text{tip}}^2 \left(\frac{R_{\text{pore}}}{R_{\text{tip}}}\right)^{\frac{9}{4}}} h^3 \tag{7}$$

Figure 8 shows the corresponding plots of eqs 1−3 and 5−7 assuming reasonable values for R_{pore}, R_{tip}, t, σ, and κ. Bending of the membrane has only a small influence on the force indentation curves as detailed above. Only if prestress or lateral tension σ is small, the response is bending dominated. Equation 5 including bending and eq 6 neglecting bending are virtually identical using σ values that roughly reproduce the experimental results for hybrid pore-spanning lipid bilayers. The finite tip size ($R_{\text{tip}} = 15$ nm) affects the curve only at larger indentation depths. Notably, the small gradient approximation limits the validity of our approach to an indentation depth of a few tenths of nanometers. Within this limit the finite tip size does not change our general argumentation based on simple plate theory.

In summary, eq 6 describes the situation for hybrid pore-spanning membranes governed exclusively by lateral tension

(23) Evans, E.; Needham, D. *J. Phys. Chem.* **1987**, *91*, 4219–4228.
(24) Needham, D.; Nunn, R. S. *Biophys. J.* **1990**, *58*, 997–1009.
(25) Landau, L. D.; Lifschitz, E. M. *Theoretische Physik, Elastizitätstheorie*; Akademie Verlag: 1991, p 66.
(26) Bhatia, N. M.; Nachbar, W. *Int. J. Non-Linear Mechanics* **1968**, *3*, 307–324.
(27) Norouzi, D.; Müller, M. M.; Deserno, M. *Phys. Rev. E* **2006**, *74*, 061914.

(e.g., prestress), while bending has to be considered to describe experiments with solvent-free supported lipid bilayers on nonfunctionalized porous silicon dioxide (eq 5). The results of the fits using eq 5 or 6 are compiled in Table 1.

Surface Functionalization. As prestress largely governs the mechanical response of the pore-spanning bilayers, which were prepared on hydrophobic thiol monolayers, we investigated the impact of the self-assembly layer on the apparent spring constant k_{app} of the membrane. Self-assembled monolayers composed of OT or CPEO3 were used for membrane preparation. Force indentation curves reveal that the average value for the apparent spring constant of nano-BLMs on CPEO3 functionalized surfaces is lower by 28% than k_{app} of nano-BLMs on OT-modified surfaces (Table 1). This decrease in k_{app} can be attributed to the imperfect nature of the CPEO3-monolayer, which allows DPhPC lipids to fill into defects of the self-assembly monolayer acting as a lipid reservoir on the pore rims. This reservoir may facilitate the membrane to flow into the pores upon indentation. The less hydrophobic nature of the monolayer might also reduce the prestress of the bilayer and, as a consequence, the apparent spring constant.

Spreading of GUVs directly on hydrophilic porous silicon substrates (solvent-free supported bilayers) results in very low apparent spring constants (Table 1, Figure 5k/l), which we attribute to a significantly reduced prestress in the membrane. The energy of adhesion, which is responsible for the prestrained membrane, is less than on hydrophobic surfaces. A water layer of a few nanometers between substrate and bilayer is usually reported. Notably, no breakthrough events were observed, which leads to the conclusion that area dilatation due to stretching is not the major contribution either. In fact, it is conceivable that the elastic response of these membranes on indentation are dominated by bending and lateral tension, which originate from the difference in free energy between the adsorbed bilayer, the lipid reservoir, and the free-standing bilayer covering the pores. Figure 5l shows the corresponding fit according to eq 5.

Membrane Phases and Lipid Composition. We also investigated the influence of the physical state of the bilayer on the elastic properties of the hybrid pore-spanning membranes. We prepared nano-BLMs composed of DPPC and varied the temperature. At 21 °C, DPPC is in the gel phase ($T_m = 41$ °C) displaying a 10 times larger bending modulus and area compressibility than at 50 °C.[29] By performing force indentation curves at 21 and 50 °C on DPPC nano-BLMs, we found a substantial decrease in the apparent spring constant from 40 mN/m at 21 °C to 9 mN/m at 50 °C (Table 1). Since we argue that the main contribution to the linear elastic response is prestress, the bending modulus influences this behavior only indirectly. Even a 10 times larger bending modulus does not shift our indentation experiments in the plate theory regime, where bending leads to a linear response. In fact, what happens is that gel-phase lipids produce a larger energy difference between the free-standing area and the phospholipid monolayer on the hydrophobic rim, resulting in a larger prestress. Since area dilatation is roughly identical for all lipid mixtures and phase states before contact with the tip, the resulting prestress is largest for gel-phase lipids due to the 10 times larger area compressibility ($\sigma = K_a(\Delta A)/(A)$). Importantly, membrane rupture of gel-phase lipids occurs at substantially higher forces but not at lower area dilatation (Figure 7). A larger fluidity also lowers the apparent lateral tension, since membrane material might flow from the rim to replenish the loss in area upon dilatation and therefore leads to a lower k_{app}. This assumption is further supported by using mixtures of DPPC and cholesterol. Addition of cholesterol to DPPC is known to reduce the bending modulus in the gel-phase and to increase it in the fluid phase. The influence of cholesterol on the prestress or more generally the apparent lateral tension depends on the bilayer phase. Mixtures of DPPC and cholesterol above the main phase transition temperature of DPPC show a larger tension, while mixtures below T_m display lower values for σ.

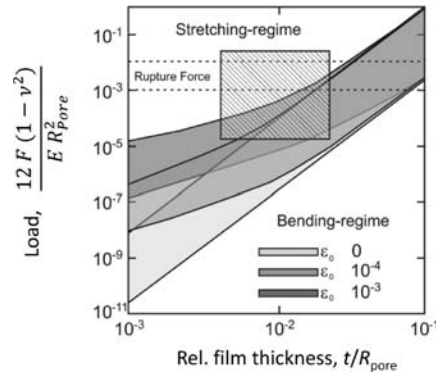

Figure 9. Illustration of relevant combinations of load and film thickness/pore radius for which either thin plate theory or nonlinear membrane theory is valid. The gray area represents the transition region between the asymptotic solutions with different prestrain ε_0.[20] The shaded box denotes the experimentally accessible regime limited also by the breakthrough of the membrane (dotted lines).

DPhPC shows a significantly larger k_{app} compared to DPPC in the fluid state in good accordance with the corresponding values for the area compressibility reported in the literature.[29,30] DPPC in the fluid state exhibits a K_a of 250 mN/m, while DPhPC displays a compressibility of $K_a = 670$ mN/m, which might be attributed to the methyl groups of the phytanoyl chains that are known to compensate for the absence of cholesterol in plants.

Solvent Content. Solvent-free DPhPC and DPPC hybrid pore-spanning bilayers were prepared from spreading GUVs on OT-covered porous substrates. It is well-known that residual organic solvent remains in the bilayer even after thinning. We found systematically higher values for σ in the absence of solvent regardless of the physical state of the bilayer. The finding can be rationalized by FRAP-experiments on solvent-free and solvent containing pore-spanning bilayers. The lateral diffusion constant is reduced by a factor of 3 in the absence of solvent, which might explain the reduced elasticity of solvent-free membranes. The presence of organic solvent reduces the prestress of the membrane, since reservoirs of solvent form at the pore boundaries. These droplets are sometimes even visible in the optical microscope.

Regimes of Elastic Behavior. In principle, membrane elasticity upon indentation can be described by linear plate theory or nonlinear membrane theory complicated by the existence of prestrain. Figure 9 illustrates the different regimes as described by Komaragiri,[20] essentially showing load as a function of film thickness assuming point load forces. The hatched box shows the accessible regime when performing force indentation curves

(28) Begley, M. R.; Mackin, T. J. *J. Mechanics Phys. Solids* **2004**, *52*, 2005–2023.
(29) Lee, C. H.; Lin, W. C.; Wang, J. P. *Phys. Rev. E* **2001**, 6402.
(30) Genova, J.; Vitkova, V.; Aladjem, L.; Meleard, P.; Mitov, M. *J. Optoelectron. Adv. Mat.* **2005**, *7*, 257–260.

on membranes on porous supports as used for this study. The breakthrough regime is indicated by two dotted lines denoting the minimal and maximal force, at which breakthrough events were observed experimentally. The transition region (gray area) is shifted to higher load at small film thickness in the presence of prestrain ε_0 ($\varepsilon_0 = [\sigma/(2K_a)]$). For supported bilayers the linear thin plate regime, where bending dominates the response, can be reached, particularly if smaller pore radii are employed. Non linear stretching, however, occurs if larger pores are used and low prestress exists.

Conclusions

The elastic response of hybrid pore-spanning membranes upon indentation with an AFM tip is mainly governed by homogeneous tension acting laterally on the pore-spanning bilayer. The free energy difference between the membrane on the pore rim and the free-standing bilayer leads to a prestress within the pore-covering membrane, which gives rise to a predominately linear force response upon indentation. The energy penalty paid for bending of the membrane is negligible if the pore diameter is larger than 200 nm. Membrane rupture occurs either spontaneously or at an area dilatation of less than 2%, confirming the assumption of a prestrained membrane. Contributions from bending dominate the elastic response of fluid bilayers only at pore radii below 20−30 nm.

The situation is significantly different for solvent-free supported bilayers deposited directly on the hydrophilic porous silicon substrate. The apparent spring constant of the membrane is several orders of magnitude lower than that of hybrid pore-spanning membranes. The prestress of the bilayer is substantially reduced and as a consequence lateral tension *and* bending dominate the mechanical response upon indentation. Membrane rupture is never observed even at an area expansion well beyond 5%.

In conclusion, the surface functionalization of the pore rims has the largest impact on the mechanical response of the free-standing bilayer and determines the response regime. Interestingly, the area dilatation of the hybrid pore-spanning bilayers is nearly identical for all lipid compositions and preparation procedures. Thereby, the measured prestress reflects the area compressibility of the bilayer and, as a consequence, the intrinsic mechanical properties of the bilayer. The reason for the differences in the apparent spring constant of the various membrane compositions is the free energy difference between the free-standing bilayer and the monolayer on top of the hydrophobic self-assembly layer.

Highest stability is reached if stochastic membrane rupture due to prestress is minimized. Hence, bilayers prepared directly from giant unilamellar vesicles on hydrophilic porous silicon exhibit highest long-term stability, albeit with the drawback of lower membrane coverage. Reaching full coverage with unstrained bilayers would provide the highest stability.

Acknowledgment. This work was supported by the DFG (JA 963/8-1 and STE 884/9-1).

Supporting Information Available: Scanning electron microscopy images of the substrate, AFM images of pore-spanning lipid bilayers, additional force indentation curves, velocity dependent indentation curves, and theoretical calculations of the elastic response of the bilayers. This material is available free of charge via the Internet at http://pubs.acs.org.

JA809165H